



# Convective transport of pulsatile multilayer hybrid nanofluid flow in a composite porous channel

Shaik Jakeer<sup>a</sup>, Seethi Reddy Reddisekhar Reddy<sup>b</sup>,  
Maduru Lakshmi Rupa<sup>c</sup>, Hayath Thameem Basha<sup>d</sup>

<sup>a</sup>School of Technology, The Apollo University,  
Chittoor, A.P, India-517127

<sup>b</sup>Department of Mathematics,  
Koneru Lakshmaiah Education Foundation,  
Bowrampet, Hyderabad 500043, Telangana, India  
[reddyshekar a43@gmail.com](mailto:red dyshekar a43@gmail.com)

<sup>c</sup>Department of Mathematics, SAS,  
Vellore Institute of Technology,  
Vellore-632014, India

<sup>d</sup>Department of Mathematical Sciences,  
Ulsan National Institute of Science and Technology,  
Ulsan, South Korea

**Received:** February 19, 2023 / **Revised:** November 6, 2023 / **Published online:** February 19, 2024

**Abstract.** Multilayer fluid models play a crucial role in comprehending fluid–fluid and fluid–nanoparticle interactions within the petroleum industry, geophysics, and plasma physics due to their diverse industrial applications. The current research aims to investigate the impact of a heat source/sink on a non-Newtonian hybrid nanofluid that saturates a porous medium positioned between a transparent viscous fluid filling a vertical channel. The model governing nonlinear coupled differential equations are nondimensionalized using appropriate fundamental quantities. Subsequently, the regular perturbation method is employed to solve the transformed dimensionless governing equations. Upon comparing the data, it is evident that current results closely align with the previously published findings. The parameter  $Q_2$  causes an increase in both  $\theta_s(\zeta)$  and  $\theta_t(\zeta)$  across all three regions. Increasing Casson parameter leads to a decrease in  $\theta_t(\zeta)$ .

**Keywords:** multilayer fluid model, porous media, hybrid nanofluid, pulsatile flow, non-Newtonian fluid, vertical channel.

## 1 Introduction or the first section

A well-known technique to alter fluids' thermal conductivity is using metal or metal oxide nanoparticles. Choi successfully carried out the studies by adding nanoparticles to the base fluid because metals have a higher thermal conductivity coefficient than common fluids, making them the most advantageous nanoparticles. According to his research, fluids

with nanoparticles have greater thermal conductivity, which speeds up heat transmission. Dharmiah et al. [6] explored the effect of nonlinear thermal radiation on an MHD nanofluid flow via a wedge with dissipative effects for Jeffrey fluid. Raza et al. [22] explore the impact of molybdenum disulfide ( $\text{MoS}_2$ ) nanoparticles morphologies on the magnetically driven fluid dynamics (MHD) flow of nanofluid in a channel with the combined effects of heat radiation and magnetic field. Several research studies on nanofluid flow were conducted [8, 18, 20, 27, 30]. Successful studies of the impact of two different types of nanoparticles in the base fluid (hybrid nanofluid) have been conducted [12, 13, 24]. Many other biological, medical, and biomechanical disciplines use the suspension of nanoparticles in blood to study biological systems [1, 26]. Photothermal therapy (PTT), a popular cancer treatment method, uses gold nanoparticles. Incoming photons are absorbed by gold nanoparticles, which then turn them into heat to destroy cancer cells. Due to their distinctive optical properties arising from localised surface plasmon resonance (LSPR), gold nanoparticles absorb light with very high efficiency (cross-section at), providing effective PTT at low radiation energy [10]. Because of the inefficient heat transfer caused by their abnormal circulatory system, tumours are more susceptible to hyperthermia than healthy tissues. Gold nanoparticles generate heat that, when exposed to light, promotes biomolecule denaturation and cellular membrane rupture, which kills tumour cells [32]. Reddy [23] looked at how bioconvection affected the flow of an electrokinetically-driven gold-copper/blood hybrid nanofluid in a horizontally uneven channel. In systems biology, which is used to treat cancer and enhance the functionality of medical equipment, entropy is estimated with the aid of this theoretical research. Chabani et al. [4] studied the magneto-hydrodynamic flow of a  $\text{Ag-Al}_2\text{O}_3/\text{H}_2\text{O}$  hybrid nanofluid in an adjusted porous trapezoidal enclosure for applications featuring the cooling of heated circular engineering systems and solidification of molten materials. Dhif et al. [7] conducted the thermal analysis for this sort of storage collector for near-steady state settings employing a nanofluid heat storage material based on  $\text{KNO}_3\text{-NaNO}_3$  binary salt combination as PCM and  $\text{Al}_2\text{O}_3\text{-SiO}_2$  nanoparticles for efficient flat plate collectors.

The fluid system used for all the above investigations consisted of only one fluid flow. Because of its many applications in research, medicine, geophysics, industry, petroleum engineering, and hydrogeology, it is important to study the dynamics of a system of two or more incompatible fluids [3, 25]. Oil recovery, blood flow through capillary vessels, equipment cleaning, biofilms and mucus flow in living cells, atmospheric carbon dioxide removal, groundwater management, crude oil flow through pipelines, bubble generation in microfluidics, and bubble trains flow in various complex porous systems are few examples of the multilayer fluid flow [2, 14]. In terms of technology, multilayer fluid models are crucial for comprehending interactions between fluids and nanoparticles and how these interactions affect flow and heat transfer properties. Nazeer et al. [19] presented a theoretical analysis of a two-phase non-Newtonian fluid with heat transfer. A brief parametric analysis of their investigation demonstrates that the channel's slick walls significantly influence the momentum of both phases. Shehzad [29] studied completely developed multilayer coatings with steady Newtonian and non-Newtonian fluids through parallel inclined plates. The primary finding is that region II's temperature and velocity profiles rose when the Jeffrey parameter grew.

In a wide spectrum of engineering and scientific systems, pulsatile flows are ubiquitous. Examples include blood circulation [15] and pulmonary ventilation in biological flows [11,21], as well as sediment transport in coastal flows, reciprocating flow in internal combustion engines [28], and movement of sediment. Although it is crucial for both knowledge expansion and technological progress, pulsatile flow turbulence still poses obstacles because of its complexity. Through the use of nozzle-style stenosis, Clark [5] examined both pulsatile and nonpulsatile flows and reported extremely disturbed flow statistics and the impact of the Reynolds number on velocity fluctuations. Non-Newtonian fluid (NNF) flows in constrained channels are of great interest in a variety of engineering and biological applications. Lee [16] and Huwang [9] are two early studies that examined laminar and simple steady flows in restricted channels. Mahapatra et al. [17] investigated irregular laminar flows in a confined space. The blood flow in a live body is inherently unstable and pulsative, which contributes to the pulse's cyclical nature. Both computational research and experimental examination of it are difficult.

A significant conclusion arises from the research gaps in previous literature: no prior investigation has delved into the heat transport and entropy generation capabilities of a titanium–gold/blood hybrid nanofluid within a multilayer flow configuration in a vertical channel. Addressing these gaps, this study explores a unique and previously uncharted facet of multilayer flow dynamics explicitly examining how porosity influences the pulsatile flow of a titanium–gold/blood hybrid nanofluid, while considering viscous dissipation and heat source effects within a porous channel. This research contributes novel insights with direct implications for various fields, including fluid dynamics, medical applications, and materials science, making it highly pertinent and pioneering in multilayer flow studies.

## 2 Mathematical formulation

Consider a convective flow in which two viscous fluid layers are squeezed together by a hybrid nanofluid layer in an infinite vertical channel. The channel is considered to be parallel to the  $x$ - and  $y$ -axis and taking perpendicular to channel. The following assumptions are taken when constructing the model. The flow has developed between three regions. The range  $-d \leq y \leq 0$ ,  $0 \leq y \leq d$ , and  $d \leq y \leq 2d$  are the regions I, II, and III, respectively. The region  $0 \leq y \leq d$  is filled with hybrid nanofluid having the viscosity  $\mu_{\text{hnf}}$ , density  $\rho_{\text{hnf}}$ , thermal conductivity  $k_{\text{hnf}}$ , the thermal expansion coefficient  $(\beta_T)_{\text{hnf}}$ , and specific heat  $(c_p)_{\text{hnf}}$ . The region  $-d \leq y \leq 0$  and  $d \leq y \leq 2d$  is filled with viscous fluid having the viscosity  $\mu_f$ , density  $\rho_f$ , thermal conductivity  $k_f$ , the thermal expansion coefficient  $(\beta_T)_f$ , and specific heat  $(c_p)_f$ . All three locations' flows are considered to be fully developed and incompressible. The fluid velocity is relatively low, this simplifies the analysis as the convective terms may be considered negligible compared to other terms in the equations. Due to buoyancy forces, the fluid rises in the channel. The left wall of the region I has the temperature  $T_{w2}$ , and right wall of the region III has the temperature  $T_{w1}$  ( $T_{w1} > T_{w2}$ ) (see Fig. 1). It is assumed that an unique unsteady pressure gradient drives the fluids in all three regions. The hybrid nanofluid flow saturated with porous matrix

with permeability  $\kappa$ . Based on the above assumptions, the governing equations can be expressed as follows [31].

Region I:

$$\begin{aligned} \frac{\partial v_1}{\partial y} &= 0, \\ \rho_f \frac{\partial u_1}{\partial t} &= -\frac{\partial P^*}{\partial x} + \mu_f \left(1 + \frac{1}{\beta}\right) \frac{\partial^2 u_1}{\partial y^2} + g(\rho_f \beta_T)_f (T_1 - T_{w2}), \\ (\rho c_p)_f \frac{\partial T_1}{\partial t} &= k_f \frac{\partial^2 T_1}{\partial y^2} + \mu_f \left(1 + \frac{1}{\beta}\right) \left(\frac{\partial u_1}{\partial y}\right)^2 + Q_1^* (T_1 - T_{w2}). \end{aligned}$$

Region II:

$$\begin{aligned} \frac{\partial v_2}{\partial y} &= 0, \\ \rho_{\text{hnf}} \frac{\partial u_2}{\partial t} &= -\frac{\partial P^*}{\partial x} + \mu_{\text{hnf}} \left(1 + \frac{1}{\beta}\right) \frac{\partial^2 u_2}{\partial y^2} + ((\rho \beta_T)_{\text{hnf}} g) (T_2 - T_{w2}) \\ &\quad - \frac{\mu_{\text{hnf}}}{\kappa} \left(1 + \frac{1}{\beta}\right) u_2, \\ (\rho c_p)_{\text{hnf}} \frac{\partial T_2}{\partial t} &= k_{\text{hnf}} \frac{\partial^2 T_2}{\partial y^2} + \mu_{\text{hnf}} \left(1 + \frac{1}{\beta}\right) \left(\frac{\partial u_2}{\partial y}\right)^2 + \frac{\mu_{\text{hnf}}}{k} \left(1 + \frac{1}{\beta}\right) u_2^2 \\ &\quad + Q_2^* (T_2 - T_{w2}). \end{aligned}$$

Region III:

$$\begin{aligned} \frac{\partial v_3}{\partial y} &= 0, \\ \rho_f \frac{\partial u_3}{\partial t} &= -\frac{\partial P^*}{\partial x} + \mu_f \left(1 + \frac{1}{\beta}\right) \frac{\partial^2 u_3}{\partial y^2} + g(\rho \beta_T)_f (T_3 - T_{w2}), \\ (\rho c_p)_f \frac{\partial T_3}{\partial t} &= k_f \frac{\partial^2 T_3}{\partial y^2} + \mu_f \left(1 + \frac{1}{\beta}\right) \left(\frac{\partial u_3}{\partial y}\right)^2 + Q_3^* (T_1 - T_{w2}). \end{aligned}$$

Boundary conditions:

$$\begin{aligned} u_1 &= 0, \quad T_1 = T_{w2} \quad \text{at } y = -d, \\ u_1 &= u_2, \quad T_1 = T_2, \\ \mu_f \left(1 + \frac{1}{\beta}\right) \frac{\partial u_1}{\partial y} &= \mu_{\text{hnf}} \left(1 + \frac{1}{\beta}\right) \frac{\partial u_2}{\partial y}, \quad k_f \frac{\partial T_1}{\partial y} = k_{\text{hnf}} \frac{\partial T_2}{\partial y} \quad \text{at } y = 0, \\ u_2 &= u_3, \quad T_2 = T_3, \\ \mu_{\text{hnf}} \left(1 + \frac{1}{\beta}\right) \frac{\partial u_2}{\partial y} &= \mu_f \left(1 + \frac{1}{\beta}\right) \frac{\partial u_3}{\partial y}, \quad k_{\text{hnf}} \frac{\partial T_2}{\partial y} = k_f \frac{\partial T_3}{\partial y} \quad \text{at } y = d, \\ u_3 &= 0, \quad T_3 = T_{w1} \quad \text{at } y = 2d, \end{aligned}$$

**Table 1.** Thermophysical properties of base fluid (blood) and nanoparticles (gold and titanium).

	Blood	Au	Ti
$\rho$ (kg m <sup>-3</sup> )	1050	19282	4510
$\beta_T$ (K <sup>-1</sup> )	$0.18 \cdot 10^{-5}$	$14 \cdot 10^{-6}$	$0.9 \cdot 10^{-5}$
$k$ (W m <sup>-1</sup> K <sup>-1</sup> )	0.52	310	20.9
$c_p$ (J kg <sup>-1</sup> K <sup>-1</sup> )	3617	129	540

where  $u_i, v_i, T_i,$  and  $Q_i^*$  ( $i = 1, 2, 3$ ) are the velocities along  $x$ -direction, the velocities along  $y$ -direction, the temperatures, and the internal heat generation/absorption of regions I, II, and III, respectively.  $\kappa$  is the porous media, and  $\beta$  is the Casson parameter. The unsteady pressure gradient is given by

$$-\frac{1}{\rho_f} \frac{\partial P^*}{\partial x} = A[1 + \varepsilon \exp(i\omega t)],$$

where  $\varepsilon \ll 1$  is a suitable chosen positive quantity,  $A$  is a known constant. Table 1 shows the thermophysical properties of blood and nanoparticles (gold and titanium) fluid. The physical characteristics of the nanofluid are defined as [32]:

$$\begin{aligned} \frac{\mu_{hnf}}{\mu_f} &= \frac{1}{(1 - \phi_{Ti})^{2.5}(1 - \phi_{Au})^{2.5}}, \\ \frac{\rho_{hnf}}{\rho_f} &= (1 - \phi_{Au}) \left( (1 - \phi_{Ti}) + \phi_{Ti} \frac{\rho_{Ti}}{\rho_f} \right) + \phi_{Au} \frac{\rho_{Au}}{\rho_f}, \\ \frac{(\rho C_p)_{hnf}}{(\rho C_p)_f} &= (1 - \phi_{Au}) \left( (1 - \phi_{Ti}) + \phi_{Ti} \frac{(\rho C_p)_{Ti}}{(\rho C_p)_f} \right) + \phi_{Au} \frac{(\rho C_p)_{Au}}{(\rho C_p)_f}, \\ \alpha_{hnf} &= \frac{k_{hnf}}{(\rho C_p)_{hnf}}, \\ \frac{(\rho \beta_t)_{hnf}}{(\rho \beta_t)_f} &= (1 - \phi_{Au}) \left( (1 - \phi_{Ti}) + \phi_{Ti} \frac{(\rho \beta_t)_{Ti}}{(\rho \beta_t)_f} \right) + \phi_{Au} \frac{(\rho \beta_t)_{Au}}{(\rho \beta_t)_f}, \\ \frac{k_{hnf}}{k_{bf}} &= \frac{(k_{Au} + (n - 1)k_{bf} - (n - 1)\phi_{Au}(k_{bf} - k_{Au}))k_{bf}}{(k_{Au} + (n - 1)k_{bf} + \phi_{Au}(k_{bf} - k_{Au}))k_f}, \end{aligned}$$

where

$$k_{bf} = \frac{k_f(k_{Ti} + (n - 1)k_f - (n - 1)\phi_{Ti}(k_f - k_{Ti}))}{k_{Ti} + (n - 1)k_f + \phi_{Ti}(k_f - k_{Ti})}.$$

Similarity transformations:

$$\begin{aligned} U_1 &= \frac{\omega u_1}{A}, & U_2 &= \frac{\omega u_2}{A}, & U_3 &= \frac{\omega u_3}{A}, \\ \theta_1 &= \frac{T_1 - T_{w2}}{T_{w1} - T_{w2}}, & \theta_2 &= \frac{T_2 - T_{w2}}{T_{w1} - T_{w2}}, & \theta_3 &= \frac{T_3 - T_{w2}}{T_{w1} - T_{w2}}, \\ P &= \frac{P^*}{A\rho_f d}, & \zeta &= \frac{y}{d}, & \eta &= \frac{x}{d}, & \tau &= \omega t, \end{aligned}$$

$$Gr = \frac{(\beta_T)_f g(T_{w1} - T_{w2}) \omega d^2}{Av_f}, \quad H^2 = \frac{\omega d^2}{v_f},$$

$$Q_1 = \frac{Q_1^* d^2}{\mu_f c_{p_f}}, \quad Q_2 = \frac{Q_2^* d^2}{\mu_f c_{p_f}}, \quad Q_3 = \frac{Q_3^* d^2}{\mu_f c_{p_f}}, \quad Pr = \frac{\mu_f (c_p)_f}{k_f}.$$

Region I:

$$H^2 \frac{\partial U_1}{\partial \tau} = -H^2 \frac{\partial P}{\partial \eta} + \left(1 + \frac{1}{\beta}\right) \frac{\partial^2 U_1}{\partial \zeta^2} + Gr \theta_1, \tag{1}$$

$$H^2 \frac{\partial \theta_1}{\partial \tau} = \frac{1}{Pr} \frac{\partial^2 \theta_1}{\partial \zeta^2} + Ec \left(1 + \frac{1}{\beta}\right) \left(\frac{\partial U_1}{\partial \zeta}\right)^2 + Q_1 \theta_1. \tag{2}$$

Region II:

$$\frac{\rho_{hnf}}{\rho_f} H^2 \frac{\partial U_2}{\partial \tau} = -H^2 \frac{\partial P}{\partial \eta} + \frac{\mu_{hnf}}{\mu_f} \left(1 + \frac{1}{\beta}\right) \frac{\partial^2 U_2}{\partial \zeta^2} + \frac{(\rho\beta_T)_{hnf}}{(\rho\beta_T)_f} Gr \theta_2, \tag{3}$$

$$-\frac{\mu_{hnf}}{\mu_f} \left(1 + \frac{1}{\beta}\right) \sigma^2 U_2 \frac{(\rho c_p)_{hnf}}{(\rho c_p)_f} H^2 \frac{\partial \theta_2}{\partial \tau}$$

$$= \frac{k_{hnf}}{k_f} \frac{1}{Pr} \frac{\partial^2 \theta_2}{\partial \zeta^2} + \frac{\mu_{hnf}}{\mu_f} \left(1 + \frac{1}{\beta}\right) Ec \left(\frac{\partial u_2}{\partial \zeta}\right)^2 + \frac{\mu_{hnf}}{\mu_f} \left(1 + \frac{1}{\beta}\right) Ec \sigma^2 U_2^2$$

$$+ Q_2 \theta_2. \tag{4}$$

Region III:

$$H^2 \frac{\partial U_3}{\partial \tau} = -H^2 \frac{\partial P}{\partial \eta} + \left(1 + \frac{1}{\beta}\right) \frac{\partial^2 U_3}{\partial \zeta^2} + Gr \theta_3, \tag{5}$$

$$H^2 \frac{\partial \theta_3}{\partial t} = \frac{1}{Pr} \frac{\partial^2 \theta_3}{\partial \zeta^2} + Ec \left(1 + \frac{1}{\beta}\right) \left(\frac{\partial U_3}{\partial \zeta}\right)^2 + Q_3 \theta_3. \tag{6}$$

The nondimensional form of the boundary conditions are:

$$U_1 = 0, \quad \theta_1 = 0 \quad \text{at } \zeta = -1,$$

$$U_1 = U_2, \quad \theta_1 = \theta_2, \quad \frac{\partial U_1}{\partial \zeta} = \frac{\mu_{hnf}}{\mu_f} \frac{\partial U_2}{\partial \zeta}, \quad \frac{\partial \theta_1}{\partial \zeta} = \frac{k_{hnf}}{k_f} \frac{\partial \theta_2}{\partial \zeta} \quad \text{at } \zeta = 0, \tag{7}$$

$$U_2 = U_3, \quad \theta_2 = \theta_3, \quad \frac{\mu_{hnf}}{\mu_f} \frac{\partial U_2}{\partial \zeta} = \frac{\partial U_3}{\partial \zeta}, \quad \frac{k_{hnf}}{k_f} \frac{\partial \theta_2}{\partial \zeta} = \frac{\partial \theta_3}{\partial \zeta} \quad \text{at } \zeta = 1,$$

$$U_3 = 0, \quad \theta_3 = 1 \quad \text{at } \zeta = 2.$$

### 3 Solution of the problem

The solution equations for  $U_i$  and  $\theta_i$  ( $i = 1, 2, 3$ ) can be written as follows [25]:

$$U_i(\zeta, t) = U_{i,1}(\zeta) + \varepsilon e^{i\omega t} U_{i,2}(\zeta), \quad \theta_i(\zeta, t) = \theta_{i,1}(\zeta) + \varepsilon e^{i\omega t} \theta_{i,2}(\zeta). \tag{8}$$

By substituting Eq. (8) into Eqs. (1)–(7) and setting the coefficients of similar powers of  $\varepsilon$  to zero, we derive the zeroth- and first-order equations along with their corresponding boundary and interface conditions as follows:

$$\left(1 + \frac{1}{\beta}\right) \left(\frac{d^2}{d\zeta^2} U_{11}(\zeta)\right) + H^2 + Gr \theta_{11}(\zeta) = 0, \quad (9)$$

$$\left(1 + \frac{1}{\beta}\right) \left(\frac{d^2}{d\zeta^2} U_{12}(\zeta)\right) - iH^2 U_{12}(\zeta) + H^2 + Gr \theta_{12}(\zeta) = 0, \quad (10)$$

$$\frac{\frac{d^2}{d\zeta^2} \theta_{11}(\zeta)}{Pr} + Q_1 \theta_{11}(\zeta) + Ec \left(1 + \frac{1}{\beta}\right) \left(\frac{d}{d\zeta} U_{11}(\zeta)\right)^2 = 0, \quad (11)$$

$$\begin{aligned} \frac{\frac{d^2}{d\zeta^2} \theta_{12}(\zeta)}{Pr} - iH^2 \theta_{12}(\zeta) + Q_1 \theta_{12}(\zeta) \\ + 2Ec \left(1 + \frac{1}{\beta}\right) \left(\frac{d}{d\zeta} U_{11}(\zeta)\right) \left(\frac{d}{d\zeta} U_{12}(\zeta)\right) = 0, \end{aligned} \quad (12)$$

$$\begin{aligned} \frac{\mu_{\text{hnf}}}{\mu_f} \left(1 + \frac{1}{\beta}\right) \left(\frac{d^2}{d\zeta^2} U_{21}(\zeta)\right) - \frac{\mu_{\text{hnf}}}{\mu_f} \left(1 + \frac{1}{\beta}\right) \sigma^2 U_{21}(\zeta) \\ + H^2 + \frac{(\rho\beta_T)_{\text{hnf}}}{(\rho\beta_T)_f} Gr \theta_{21}(\zeta) = 0, \end{aligned} \quad (13)$$

$$\begin{aligned} \frac{\mu_{\text{hnf}}}{\mu_f} \left(1 + \frac{1}{\beta}\right) \left(\frac{d^2}{d\zeta^2} U_{22}(\zeta)\right) - i\frac{\rho_{\text{hnf}}}{\rho_f} H^2 U_{22}(\zeta) \\ - \frac{\mu_{\text{hnf}}}{\mu_f} \left(1 + \frac{1}{\beta}\right) \sigma^2 U_{22}(\zeta) + H^2 + \frac{(\rho\beta_T)_{\text{hnf}}}{(\rho\beta_T)_f} Gr \theta_{22}(\zeta) = 0, \end{aligned} \quad (14)$$

$$\begin{aligned} \frac{k_{\text{hnf}}}{k_f} \frac{1}{Pr} \left(\frac{d^2}{d\zeta^2} \theta_{21}(\zeta)\right) + \frac{\mu_{\text{hnf}}}{\mu_f} Ec \left(1 + \frac{1}{\beta}\right) \left(\frac{d}{d\zeta} U_{21}(\zeta)\right)^2 \\ + \frac{\mu_{\text{hnf}}}{\mu_f} Ec \left(1 + \frac{1}{\beta}\right) \sigma^2 U_{21}^2(\zeta) + Q_2 \theta_{21}(\zeta) = 0, \end{aligned} \quad (15)$$

$$\begin{aligned} \frac{k_{\text{hnf}}}{k_f} \frac{1}{Pr} \left(\frac{d^2}{d\zeta^2} \theta_{22}(\zeta)\right) + 2\frac{\mu_{\text{hnf}}}{\mu_f} Ec \left(1 + \frac{1}{\beta}\right) \left(\frac{d}{d\zeta} U_{21}(\zeta)\right) \left(\frac{d}{d\zeta} U_{22}(\zeta)\right) \\ - i\frac{(\rho c_p)_{\text{hnf}}}{(\rho c_p)_f} H^2 \theta_{22}(\zeta) + Q_2 \theta_{22}(\zeta) \\ + 2\frac{\mu_{\text{hnf}}}{\mu_f} Ec \left(1 + \frac{1}{\beta}\right) \sigma^2 U_{21}(\zeta) U_{22}(\zeta) = 0, \end{aligned} \quad (16)$$

$$\left(1 + \frac{1}{\beta}\right) \left(\frac{d^2}{d\zeta^2} U_{31}(\zeta)\right) + H^2 + Gr \theta_{31}(\zeta) = 0, \quad (17)$$

$$\left(1 + \frac{1}{\beta}\right) \left(\frac{d^2}{d\zeta^2} U_{32}(\zeta)\right) - iH^2 U_{32}(\zeta) + H^2 + Gr \theta_{32}(\zeta) = 0, \quad (18)$$

$$\frac{1}{Pr} \frac{d^2}{d\zeta^2} \theta_{31}(\zeta) + Q_3 \theta_{31}(\zeta) + Ec \left(1 + \frac{1}{\beta}\right) \left(\frac{d}{d\zeta} U_{31}(\zeta)\right)^2 = 0, \quad (19)$$

$$\begin{aligned} & \frac{1}{Pr} \frac{d^2}{d\zeta^2} \theta_{32}(\zeta) - iH^2 \theta_{32}(\zeta) + Q_3 \theta_{32}(\zeta) \\ & + 2Ec \left(1 + \frac{1}{\beta}\right) \left(\frac{d}{d\zeta} U_{31}(\zeta)\right) \left(\frac{d}{d\zeta} U_{32}(\zeta)\right) = 0 \end{aligned} \quad (20)$$

with boundary conditions

$$U_{11} = 0, \quad \theta_{11} = 0, \quad U_{12} = 0, \quad \theta_{12} = 0 \quad \text{at } \zeta = -1,$$

$$U_{11} = U_{21}, \quad \theta_{11} = \theta_{21},$$

$$\frac{\partial U_{11}}{\partial \zeta} = \frac{\mu_{hnf}}{\mu_f} \frac{\partial U_{21}}{\partial \zeta}, \quad \frac{\partial \theta_{11}}{\partial \zeta} = \frac{k_{hnf}}{k_f} \frac{\partial \theta_{21}}{\partial \zeta} \quad \text{at } \zeta = 0,$$

$$U_{12} = U_{22}, \quad \theta_{12} = \theta_{22},$$

$$\frac{\partial U_{12}}{\partial \zeta} = \frac{\mu_{hnf}}{\mu_f} \frac{\partial U_{22}}{\partial \zeta}, \quad \frac{\partial \theta_{12}}{\partial \zeta} = \frac{k_{hnf}}{k_f} \frac{\partial \theta_{22}}{\partial \zeta} \quad \text{at } \zeta = 0,$$

$$U_{21} = U_{31}, \quad \theta_{21} = \theta_{31},$$

$$\frac{\mu_{hnf}}{\mu_f} \frac{\partial U_{21}}{\partial \zeta} = \frac{\partial U_{31}}{\partial \zeta}, \quad \frac{k_{hnf}}{k_f} \frac{\partial \theta_{21}}{\partial \zeta} = \frac{\partial \theta_{31}}{\partial \zeta} \quad \text{at } \zeta = 1,$$

$$U_{22} = U_{32}, \quad \theta_{22} = \theta_{32},$$

$$\frac{\mu_{hnf}}{\mu_f} \frac{\partial U_{22}}{\partial \zeta} = \frac{\partial U_{32}}{\partial \zeta}, \quad \frac{k_{hnf}}{k_f} \frac{\partial \theta_{22}}{\partial \zeta} = \frac{\partial \theta_{32}}{\partial \zeta} \quad \text{at } \zeta = 1,$$

$$U_{31} = 0, \quad \theta_{31} = 1, \quad U_{32} = 0, \quad \theta_{32} = 1 \quad \text{at } \zeta = 2.$$

Since the solutions of Eqs. (9)–(20) along with their boundary interface conditions can be found easily by integrating the equations (see Umavathi and Hemavathi [31]).

The dimensionless Nusselt number is given by

$$Nu = -(\theta'_i)_{\zeta=-1,2} = -(\theta'_{i,1} + \varepsilon \theta'_{i,2} e^{it})_{\zeta=-1,2}, \quad \text{where } i = 1, 3.$$

## 4 Results and discussion

The purpose of this section is to depict the convective transport of pulsatile multilayer flow of titanium (Ti) and gold (Au) based blood hybrid nanofluid in a composite porous channel with thermal radiation and heat source/sink parameters in three different regions effects. It is assumed that the momentum and thermal aspects of hybrid across the contact are all uninterrupted. Using the perturbation approach, analytical calculations have been done to analyze the multifluid model for several relevant parameters, including the Casson parameter  $\beta$ , Grashof number  $Gr$ , frequency parameter  $H$ , porous parameter  $\sigma$ , Eckert

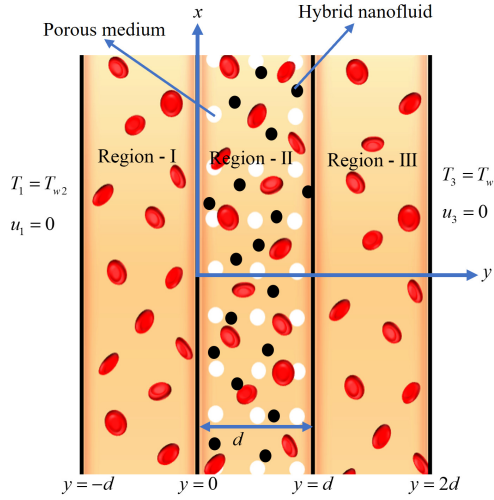


Figure 1. Geometry of the problem.

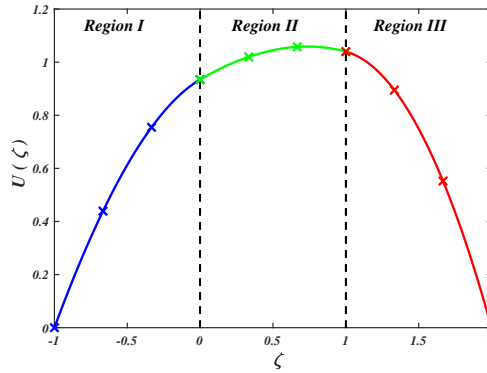
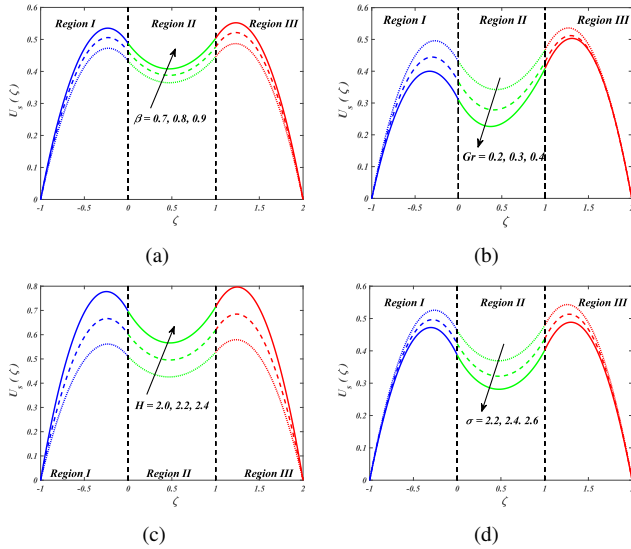


Figure 2. Comparison of present results with Umavati and Hemavati [31].

number  $Ec$ , nanoparticle volume fraction  $\phi = \phi_{Au} + \phi_{Ti} = 0.05$ , heat source/sink parameters  $Q_1, Q_2$ , and  $Q_3$ , time  $t$  on Ti–Au/ blood hybrid nanofluid velocities  $U_s(\zeta)$  and  $U_t(\zeta)$  and temperature  $\theta_s(\zeta)$  and  $\theta_t(\zeta)$  are visualized and elaborately discussed. Figure 1 shows the three different heat source/sink parameter regions. The first region between  $-1$  and  $0$  is blue, the second region between  $0$  and  $1$  is green, and the third region between  $1$  and  $2$  is red, respectively. Figure 2 shows the comparison of present results with Umavati and Hemavati [31]. The results show good agreement with the Umavati and Hemavati [31].

Figures 3(a)–3(d) manifested the steady velocity profiles  $U_s(\zeta)$  for Casson parameter ( $\beta = 0.7, 0.8, 0.9$ ), Grashof number ( $Gr = 0.2, 0.3, 0.4$ ), frequency parameter ( $H = 2.0, 2.2, 2.4$ ), porous parameter ( $\sigma = 2.2, 2.4, 2.6$ ) through three different regions. Figure 3(a) demonstrates that improving Casson parameter  $\beta$  tend to increase the  $U_s(\zeta)$ .



**Figure 3.** Steady velocity profiles for different values of (a) Casson parameter  $\beta$ , (b) Grashof number  $Gr$ , (c) frequency parameter  $H$ , and (d) porous parameter  $\sigma$ .

This is due to the fact that an increase in  $\beta$  creates a rise in fluid viscosity, and it follows that a greater viscosity produces a larger velocity. The extent of the growth, however, differs depending on the region. The amplitude of the velocity increase is less in region II when compared to the region I and in region II when compared to region III because the fluid is saturated with porous medium in the middle of the channel. The Casson parameter within the velocity profile can be relevant for understanding blood flow dynamics, particularly during cardiac cycles. By adjusting this parameter, researchers can model the impact of non-Newtonian behavior on blood flow in arteries and predict changes in shear stress, which is vital for assessing the risk of cardiovascular diseases. Figure 3(b) displays how the  $U_s(\zeta)$  profile and  $Gr$  is inversely connected. This graph demonstrates that the velocity profiles decrease with increasing amounts of Grashof number. However, the rate of expansion varies depending on the area. Because the fluid is saturated with porous medium in the center of the channel, the amplitude of the velocity increase is smaller in region II than in region I and in region II than in region III. In Fig. 3(c) the behavior of the  $H$  on velocity  $U_s(\zeta)$  is portrayed. This graph demonstrates that the higher values of  $H$  increase all three regions of the  $U_s(\zeta)$ . Physically, this corresponds to the ratio of pulsatile flow oscillation frequency to body acceleration frequency. However, compared to the centre of the channel, the effect of augmentation on the velocity field is more pronounced towards the right and left walls of the channel. Figure 3(d) illustrates how the porous parameter  $\sigma$  influences on velocity profile  $U_s(\zeta)$ . According to this graph,  $U_s(\zeta)$  is diminished by expanding values in the  $\sigma$ . Physically, the porous media causes the fluid motion to produce second-order quadratic drag, which lowers the velocity in the boundary layer. Comparing region I and region III to the mid-channel (nanofluid saturated with porous media), the impact of suppression is dominant (clear viscous). When the

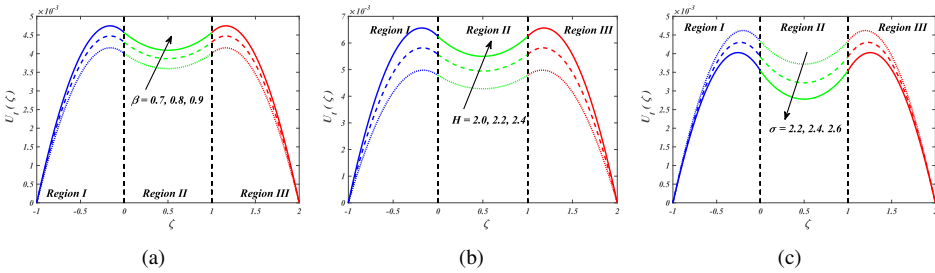


**Figure 4.** Unsteady velocity profiles for different values of (a) Casson parameter  $\beta$ , (b) frequency parameter  $H$ , and (c) porous parameter  $\sigma$ .

tube is completely filled with one fluid, this is another typical outcome that is seen. This parameter adjustment helps in modeling the behavior of fluids in tissues or porous structures during dynamic processes, such as pulsatile blood flow in arteries. Lowering the porous parameter can represent changes in tissue elasticity or permeability, aiding in the understanding of diseases like hypertension, arteriosclerosis, and tumor growth within porous tissues.

The consequence of the Casson parameter ( $\beta = 0.7, 0.8, 0.9$ ), frequency parameter ( $H = 2.0, 2.2, 2.4$ ), and porous parameter ( $\sigma = 2.2, 2.4, 2.6$ ) over three different regions on unsteady velocity  $U_t(\zeta)$  is represented in Figs. 4(a)–4(c). Figure 4(a) illustrates how the Casson parameter  $\beta$  influence on velocity profile  $U_t(\zeta)$ . According to this graph,  $U_t(\zeta)$  is augmented by expanding values in  $\beta$ . Physically, an increase in  $\beta$  creates a rise in fluid viscosity, and it follows that a greater viscosity produces a larger velocity. Comparing region I and region III to the mid-channel (nanofluid saturated with porous media), the impact of suppression is dominant (clear viscous). When the tube is completely filled with one fluid, this is another typical outcome that is seen. Figure 4(b) demonstrates that improving frequency parameter  $H$  tends to increase the  $U_t(\zeta)$ . Physically, this corresponds to the ratio of pulsatile flow oscillation frequency to body acceleration frequency. The extent of the growth, however, differs depending on the region. The amplitude of the velocity increase is less in region II when compared to the region I and in region II when compared to region III because the fluid is saturated with porous medium in the middle of the channel. This modification may indicate disorders such as bradycardia or other heart rhythm irregularities, delivering information about the influence on hemodynamics as well as possible health concerns. Understanding these slower frequency patterns is critical in diagnosing, controlling, and forecasting the consequences of cardiac diseases on blood flow and tissue perfusion. In Fig. 4(c) the behavior of  $\sigma$  on velocity  $U_t(\zeta)$  is portrayed. This graph demonstrates that the higher values of  $\sigma$  diminish all three regions of  $U_t(\zeta)$ . Physically, the porous media causes the fluid motion to produce second-order quadratic drag, which lowers the velocity in the boundary layer. However, compared to the centre of the channel, the effect of augmentation on the velocity field is more pronounced towards the right and left walls of the channel.

Figures 5(a)–5(f) manifesting the steady temperature profiles  $\theta_s(\zeta)$  has been examined for Casson parameter ( $\beta = 0.7, 0.8, 0.9$ ), frequency parameter ( $H = 2.0, 2.2, 2.4$ ),

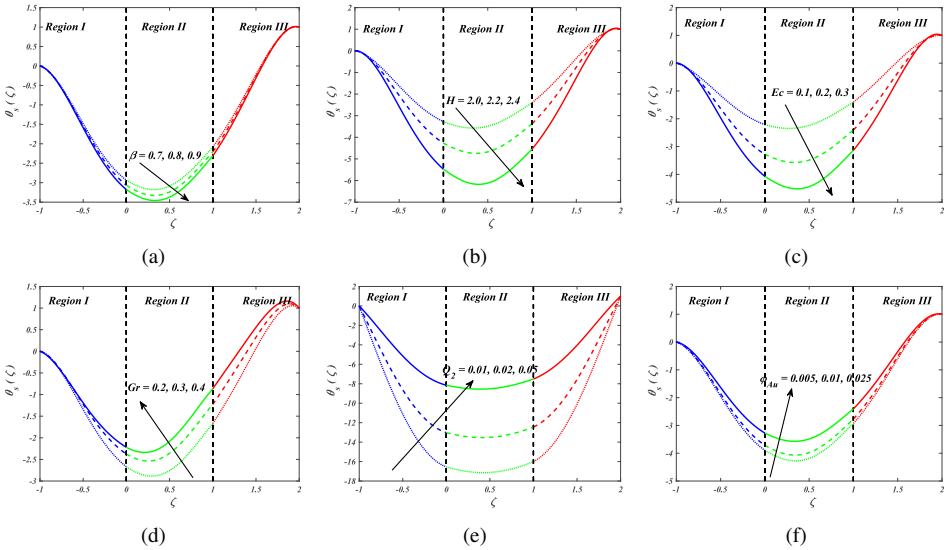


**Figure 5.** Steady temperature profiles for different values of (a) Casson parameter  $\beta$ , (b) frequency parameter  $H$ , (c) Eckert number  $Ec$ , (d) Grashof number  $Gr$ , (e) heat source/sink parameters  $Q_2$ , and (f) nanoparticle volume fraction  $\phi_{Au}$ .

Eckert number ( $Ec = 0.1, 0.2, 0.3$ ), Grashof number ( $Gr = 0.2, 0.3, 0.4$ ), heat source/sink parameters ( $Q_2 = 0.01, 0.02, 0.05$ ), and nanoparticle volume fraction ( $\phi = 0.005, 0.010, 0.025$ ) through three different regions. Figure 5(a) demonstrates that improving Casson parameter  $\beta$  tends to diminution of  $\theta_s(\zeta)$ . This is due to the fact that an decrease in  $\beta$  creates a rise in fluid temperature, and it follows that a lesser viscosity produces a larger temperature. The extent of the growth, however, differs depending on the region. The amplitude of the temperature increase is less in region II when compared to the region I and in region II when compared to region III because the fluid is saturated with porous medium in the middle of the channel. In Fig. 5(b) the behavior of the  $H$  on temperature profiles  $\theta_s(\zeta)$  is portrayed. This graph demonstrates that the higher values of  $H$  reduce all three regions of the  $\theta_s(\zeta)$ . Physically, this corresponds to the ratio pulsatile flow oscillation frequency to body acceleration frequency. However, compared to the centre of the channel, the effect of diminution on the temperature is more pronounced towards the right and left walls of the channel. In Fig. 5(c) the behavior of  $Ec$  on temperature profiles  $\theta_s(\zeta)$  is portrayed. This graph demonstrates that the higher values of  $Ec$  reduce all three regions of  $\theta_s(\zeta)$ . Physically, the higher  $Ec$  produces more kinetic energy, causing particles to collide more frequently and dissipate energy. As a result, kinetic energy is converted into thermal energy. However, compared to the centre of the channel, the effect of diminution on the temperature is more pronounced towards the right and left walls of the channel. Figure 5(d) displays how  $\theta_s(\zeta)$  profile and  $Gr$  are inversely connected. This graph demonstrates the temperature profile intensifications with increasing amounts of Grashof number. However, the rate of expansion varies depending on the area. Because the fluid is saturated with porous medium in the center of the channel, the amplitude of

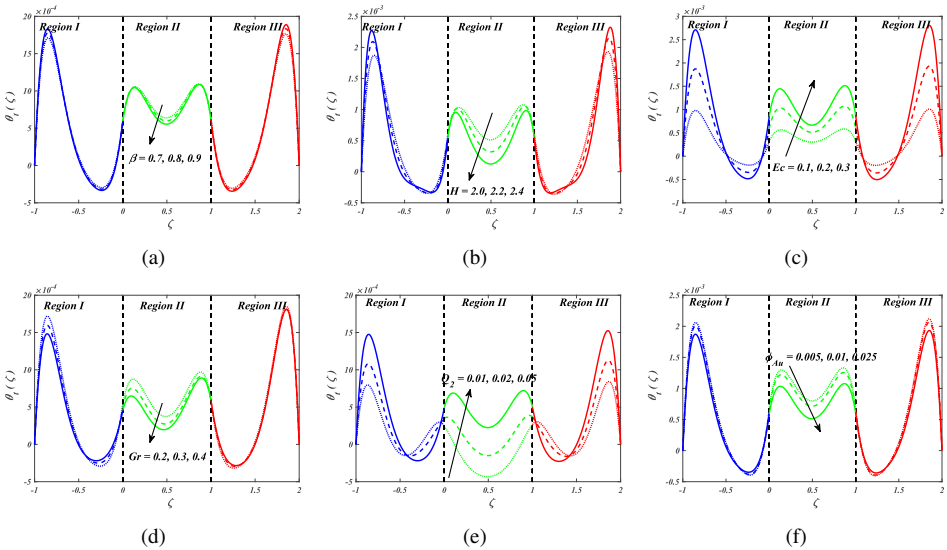


**Figure 6.** Unsteady temperature profiles for different values of (a) Casson parameter  $\beta$ , (b) frequency parameter  $H$ , (c) Eckert number  $Ec$ , (d) Grashof number  $Gr$ , (e) heat source/sink parameters  $Q_2$ , and (f) nanoparticle volume fraction  $\phi_{Au}$ .

the temperature increase is smaller in region II than in region I and in region II than in region III. In Fig. 5(e) the behavior of  $Q_2$  on temperature  $\theta_s(\zeta)$  is portrayed. This graph demonstrates that the higher values of  $Q_2$  increase all three regions of the  $\theta_s(\zeta)$ . However, compared to the centre of the channel, the effect of augmentation on the velocity field is more pronounced towards the right and left walls of the channel. It depicts situations when the amount of heat input or removal changes over time, such as when a person’s body temperature is controlled by a fever or while receiving thermal therapy for medical conditions. Understanding how this parameter fluctuation affects different medical applications, such as hyperthermia therapies and thermal ablation techniques for tumor therapy, aids in the optimization of thermal management tactics. In Fig. 5(f) the behavior of  $\phi_{Au}$  on temperature profiles  $\theta_s(\zeta)$  is portrayed. This graph demonstrates that the higher values of  $\phi_{Au}$  rises all three regions of  $\theta_s(\zeta)$ . One may explain this outcome by claiming that when nanoparticles are introduced to pure fluid, the fluid’s density rises, and the fluid becomes denser, which causes the fluid’s momentum to increase in the channel. However, compared to the centre of the channel, the effect of diminution on the temperature is more pronounced towards the right and left walls of the channel.

Figures 6(a)–6(f) manifesting the unsteady temperature profiles  $\theta_t(\zeta)$  has been examined for Casson parameter ( $\beta = 0.7, 0.8, 0.9$ ), frequency parameter ( $H = 2.0, 2.2, 2.4$ ), Eckert number ( $Ec = 0.1, 0.2, 0.3$ ), Grashof number ( $Gr = 0.2, 0.3, 0.4$ ), heat source/sink parameters ( $Q_2 = 0.01, 0.02, 0.05$ ), and nanoparticle volume fraction ( $\phi = 0.005, 0.010, 0.025$ ) through three different regions. Figure 6(a) demonstrates that improving Casson parameter  $\beta$  tends to diminution of  $\theta_t(\zeta)$ . This is due to the fact that an decrease in  $\beta$  creates a rise in fluid temperature, and it follows that a lesser viscosity produces

a larger temperature. The extent of the growth, however, differs depending on the region. The amplitude of the temperature increase is less in region II when compared to the region I and in region II when compared to region III because the fluid is saturated with porous medium in the middle of the channel. In Fig. 6(b) the behavior of the  $H$  on temperature profiles  $\theta_t(\zeta)$  is portrayed. This graph demonstrates that the higher values of  $H$  reduce all three regions of the  $\theta_t(\zeta)$ . Physically, this corresponds to the ratio of pulsatile flow oscillation frequency to body acceleration frequency. However, compared to the centre of the channel, the effect of diminution on the temperature is more pronounced towards the right and left walls of the channel. Lower frequency thermal fluctuations or slower temperature oscillations are indicated by a drop in the frequency parameter within the temperature profile. When simulating biological or environmental systems that experience moderate temperature fluctuations, such as seasonal climatic changes or the circadian cycles of living things, this adjustment may be important. In disciplines like ecology, physiology, and climate science, being able to predict temperature-related phenomena with accuracy is crucial. It can also help in the creation of controlled environments for a variety of uses, such as farming, medical research, and climate studies. In Fig. 6(c) the behavior of the  $Ec$  on temperature profiles  $\theta_t(\zeta)$  is portrayed. This graph demonstrates that the higher values of  $Ec$  intensify all three regions of the  $\theta_t(\zeta)$ . Physically, the higher  $Ec$  produces more kinetic energy, causing particles to collide more frequently and dissipate energy. As a result, kinetic energy is converted into thermal energy. However, compared to the centre of the channel, the effect of diminution on the temperature is more pronounced towards the right and left walls of the channel. Figure 6(d) displays how  $\theta_t(\zeta)$  profile and  $Gr$  are inversely connected. This graph demonstrates the temperature profile diminutions with increasing amounts of Grashof number. However, the rate of expansion varies depending on the area. Because the fluid is saturated with porous medium in the center of the channel, the amplitude of the temperature increase is smaller in region II than in region I and in region II than in region III. The reduction in the Grashof number within the temperature profile corresponds to situations with less buoyancy-driven heat transfer. When modeling scenarios with smaller temperature gradients, such as regulated cooling operations in medical equipment like refrigeration units for storing temperature-sensitive drugs or organ preservation, this modification could be important. For accurate temperature management in medical and pharmaceutical applications, protecting the integrity of delicate biological materials and medicines, it is essential to comprehend the impact of a lower Grashof number. In Fig. 6(e) the behavior of the  $Q_2$  on temperature  $\theta_t(\zeta)$  is portrayed. This graph demonstrates that the higher values of  $Q_2$  increase all three regions of  $\theta_t(\zeta)$ . However, compared to the centre of the channel, the effect of augmentation on the velocity field is more pronounced towards the right and left walls of the channel. In Fig. 6(f) the behavior of the  $\phi_{Au}$  on temperature profiles  $\theta_t(\zeta)$  is portrayed. This graph demonstrates the higher values of  $\phi_{Au}$  reductions all three regions of  $\theta_t(\zeta)$ . One may explain this outcome by claiming that when nanoparticles are introduced to pure fluid, the fluid's density rises, and the fluid becomes denser, which causes the fluid's momentum to increase in the channel. However, compared to the centre of the channel, the effect of diminution on the temperature is more pronounced towards the right and left walls of the channel. The nanoparticle dispersion in a fluid changes over time, such as in drug delivery with temperature-sensitive

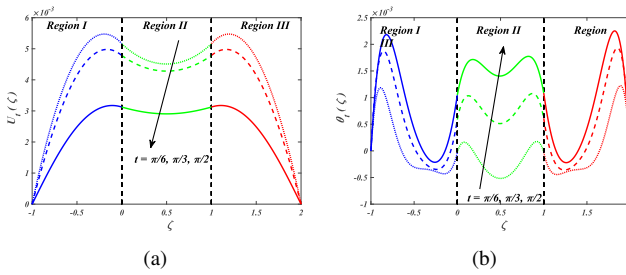


**Figure 7.** Effect of time  $t$  on (a) unsteady velocity profile and (b) unsteady temperature profile.

**Table 2.** Values of  $Nu$  for different values of  $\beta$ ,  $Gr$ , and  $\sigma$  with  $\phi_{Au} = \phi_{Ti} = 0$ ,  $Ec = Q_1 = Q_2 = Q_3 = 0.1$ ,  $t = \pi/3$ , and  $H = 1$ .

$\beta$	$Gr$	$\sigma$	$Nu$	
			$\zeta = -1$	$\zeta = 2$
0.5	0	0	1.46183	-0.46422
1.0	0	0	1.41708	-0.41947
inf	0	0	1.28284	-0.28523
0.5	0.1	0	1.47938	-0.43674
1.0	0.1	0	1.44314	-0.37846
inf	0.1	0	1.33382	-0.20460
0.5	0	2	1.72231	-0.72470
1.0	0	2	1.80780	-0.81019
inf	0	2	2.06429	-1.06668

nanoparticles. Understanding how this parameter affects heat transfer is crucial for optimizing applications like targeted hyperthermia treatments and controlled drug release within biological systems, ensuring the safety and effectiveness of these therapies.

Figures 7(a) and 7(b) manifesting the unsteady velocity  $U_t(\zeta)$  and unsteady temperature profiles  $\theta_t(\zeta)$  has been examined for time series parameter ( $t = \pi/6, \pi/3, \pi/2$ ) through three different regions. In Fig. 7(a) the behavior of  $Q_2$  on temperature  $U_t(\zeta)$  is portrayed. This graph demonstrates that the higher values of  $t$  diminish all three regions of  $U_t(\zeta)$ . However, the rate of expansion varies depending on the area. Because the fluid is saturated with porous medium in the center of the channel, the amplitude of the temperature increase is smaller in region II than in region I and in region II than in region III. Figure 7(b) displays how  $\theta_t(\zeta)$  profile and  $t$  are inversely connected. This graph demonstrates the temperature profile developments with increasing amounts of  $t$ . The amplitude of the temperature increase is less in region II when compared to the region I and in region II when compared to region III because the fluid is saturated with porous medium in the middle of the channel.

At  $\zeta = -1$  and  $\zeta = 2$ , the outcomes of  $Nu$  for diverse aspects of  $\beta$ ,  $Gr$ , and  $\sigma$  with Au–Ti hybrid nanofluids are taken as absent (see Table 2). From this we observed that  $Nu$  increases in  $\zeta = -1$  with various values of  $\beta$ ,  $Gr$ , and  $\sigma$ . In Table 3, at  $\zeta = -1$  and  $\zeta = 2$ , the outcomes of  $Nu$  for diverse aspects of  $\beta$ ,  $H$ ,  $Gr$ ,  $Ec$ ,  $Q_1$ ,  $Q_2$ ,  $Q_3$ , and  $\sigma$  with Au–Ti hybrid nanofluids are taken as 0.025 and  $t = \pi/3$ . From this we observed that  $Nu$  diminishes the larger values of  $Ec$ ,  $Q_1$ ,  $Q_2$ , and  $Q_3$ .

**Table 3.** Values of  $Nu$  for different values of  $H, Gr, \sigma, Ec, Q_1, Q_2,$  and  $Q_3$  with  $\phi_{Au} = \phi_{Ti} = 0.025$  and  $t = \pi/3$ .

$\beta$	$H$	$Gr$	$\sigma$	$Ec$	$Q_1$	$Q_2$	$Q_3$	$Nu$	
								$\zeta = -1$	$\zeta = 2$
0.5	2.0	0.1	2.0	0.20	0.10	0.20	0.10	0.79656	0.42256
1.0	2.0	0.1	2.0	0.20	0.10	0.20	0.10	0.55100	0.82082
1.5	2.0	0.1	2.0	0.20	0.10	0.20	0.10	0.37220	1.09330
1.0	0.5	0.1	2.0	0.20	0.10	0.20	0.10	0.90581	0.03709
1.0	1.0	0.1	2.0	0.20	0.10	0.20	0.10	0.94120	0.08734
1.0	1.5	0.1	2.0	0.20	0.10	0.20	0.10	0.91409	0.25627
1.0	2.0	0.2	2.0	0.20	0.10	0.20	0.10	0.38569	1.46968
1.0	2.0	0.3	2.0	0.20	0.10	0.20	0.10	0.47236	1.92933
1.0	2.0	0.4	2.0	0.20	0.10	0.20	0.10	0.71853	2.44020
1.0	2.0	0.1	2.5	0.20	0.10	0.20	0.10	0.83971	0.49118
1.0	2.0	0.1	3.0	0.20	0.10	0.20	0.10	0.88825	0.40958
1.0	2.0	0.1	3.5	0.20	0.10	0.20	0.10	0.82258	0.43953
1.0	2.0	0.1	2.0	0.05	0.10	0.20	0.10	0.96929	0.06229
1.0	2.0	0.1	2.0	0.10	0.10	0.20	0.10	0.89431	0.24939
1.0	2.0	0.1	2.0	0.15	0.10	0.20	0.10	0.74687	0.50994
1.0	2.0	0.1	2.0	0.20	0.11	0.20	0.10	0.78130	1.02362
1.0	2.0	0.1	2.0	0.20	0.12	0.20	0.10	1.03618	1.24281
1.0	2.0	0.1	2.0	0.20	0.13	0.20	0.10	1.31938	1.48079
1.0	2.0	0.1	2.0	0.20	0.10	0.17	0.10	1.27100	-0.00377
1.0	2.0	0.1	2.0	0.20	0.10	0.18	0.10	1.00897	0.29162
1.0	2.0	0.1	2.0	0.20	0.10	0.19	0.10	0.76983	0.56557
1.0	2.0	0.1	2.0	0.20	0.10	0.20	0.12	0.36255	0.76575
1.0	2.0	0.1	2.0	0.20	0.10	0.20	0.13	0.25859	0.72530
1.0	2.0	0.1	2.0	0.20	0.10	0.20	0.14	0.14691	0.67433

### 5 Conclusion

This study aims to determine the influence of a heat source/sink on a non-Newtonian hybrid nanofluid saturated with a porous medium separated between the transparent viscous fluid filled in a vertical channel. The main goal of this research is to depict the blood-based nanofluid flow properties after the mechanism has been filled with nanoparticles. The influence of distinctive factors like the Casson parameter, Grashof number, frequency parameter, porous parameter, Eckert number, nanoparticle volume fraction, heat source/sink parameters, and time parameter are shown through two-dimensional graphs and tables. The following significant findings emerged from this investigation:

- Improving Casson parameter  $\beta$  tends to increase the steady  $U_s(\zeta)$  and unsteady velocity profiles  $U_t(\zeta)$ .
- Velocity profiles decrease with increasing amounts of Grashof number, and the opposite nature is observed for the temperature profiles.
- The velocity profile  $U_s(\zeta)$  is diminished by expanding values in the porosity parameter  $\sigma$ .
- The higher values of  $t$  diminish all three regions of the  $U_t(\zeta)$ , and the contrary nature is detected for  $\theta_t(\zeta)$ .

- The heat source/sink parameter  $Q_2$  increases all three regions of  $\theta_s(\zeta)$  and  $\theta_t(\zeta)$ .
- The frequency parameter  $H$  reduces all three regions of  $\theta_t(\zeta)$  and  $\theta_s(\zeta)$ .

## References

1. A. Abbasi, W. Farooq, E.S.M. Tag-ElDin, S.U. Khan, M.I. Khan, K. Guedri, S. Elattar, M. Waqas, A.M. Galal, Heat transport exploration for hybrid nanoparticle (Cu,  $\text{Fe}_3\text{O}_4$ )—Based blood flow via tapered complex wavy curved channel with slip features, *Micromachines*, **13**(9):1415, 2022, <https://doi.org/10.3390/mi13091415>.
2. A.K. Alzahrani, Z. Abbas, M.Z. Ullah, Chemically reactive two-phase flow of viscous-Casson fluids in a rotating channel, *Alexandria Eng. J.*, **62**:403–413, 2023, <https://doi.org/10.1016/J.AEJ.2022.07.036>.
3. T. Anwar, Asifa, P. Kumam, A fractal fractional model for thermal analysis of GO – NaAlG – Gr hybrid nanofluid flow in a channel considering shape effects, *Case Stud. Therm. Eng.*, **31**:101828, 2022, <https://doi.org/10.1016/J.CSITE.2022.101828>.
4. I. Chabani, F. Mebarek-Oudina, H. Vaidya, A.I. Ismail, Numerical analysis of magnetic hybrid nano-fluid natural convective flow in an adjusted porous trapezoidal enclosure, *J. Magn. Magn. Mater.*, **564**:170142, 2022, <https://doi.org/10.1016/j.jmmm.2022.170142>.
5. C. Clark, The fluid mechanics of aortic stenosis—I. Theory and steady flow experiments, *J. Biomech.*, **9**(8):521–528, 1976, [https://doi.org/10.1016/0021-9290\(76\)90068-3](https://doi.org/10.1016/0021-9290(76)90068-3).
6. G. Dharmiah, F. Mebarek-Oudina, M.S. Kumar, K.C. Kala, Nuclear reactor application on Jeffrey fluid flow with Falkner-skann factor, Brownian and thermophoresis, non linear thermal radiation impacts past a wedge, *J. Indian Chem. Soc.*, **100**(2):100907, 2023, <https://doi.org/10.1016/j.jics.2023.100907>.
7. K. Dhif, F. Mebarek-Oudina, S. Chouf, H. Vaidya, A.J. Chamkha, Thermal analysis of the solar collector cum storage system using a hybrid-nanofluids, *J. Nanofluids*, **10**(4):616–626, 2021, <https://doi.org/10.1166/jon.2021.1807>.
8. A.S. Dogonchi, M.K. Nayak, N. Karimi, A.J. Chamkha, D.D. Ganji, Numerical simulation of hydrothermal features of Cu– $\text{H}_2\text{O}$  nanofluid natural convection within a porous annulus considering diverse configurations of heater, *J. Therm. Anal. Calorim.*, **141**:2109–2125, 2020, <https://doi.org/10.1007/s10973-020-09419-y>.
9. H. Huang, B.R. Seymour, A finite difference method for flow in a constricted channel, *Computers Fluids*, **24**(2):153–160, 1995, [https://doi.org/10.1016/0045-7930\(94\)00022-Q](https://doi.org/10.1016/0045-7930(94)00022-Q).
10. S. Jain, D.G. Hirst, J.M. O’Sullivan, Gold nanoparticles as novel agents for cancer therapy, *Br. J. Radiol.*, **85**(1010):113, 2012, <https://doi.org/10.1259/BJR/59448833>.
11. F. Jiang, T. Hirano, J. Ohgi, X. Chen, A voxel image-based pulmonary airflow simulation method with an automatic detection algorithm for airway outlets, *Int. J. Numer. Methods Biomed. Eng.*, **36**(3):e3305, 2020, <https://doi.org/10.1002/CNM.3305>.
12. M.I. Khan, S. Qayyum, F. Shah, R.N. Kumar, R.J.P. Gowda, B.C. Prasannakumara, Y.M. Chu, S. Kadry, Marangoni convective flow of hybrid nanofluid ( $\text{MnZnFe}_2\text{O}_4$  –  $\text{NiZnFe}_2\text{O}_4$  –  $\text{H}_2\text{O}$ ) with Darcy Forchheimer medium, *Ain Shams Eng. J.*, **12**(4):3931–3938, 2021, <https://doi.org/10.1016/j.asej.2021.01.028>.

13. U. Khan, F. Mebarek-Oudina, A. Zaib, A. Ishak, S. Abu Bakar, E.S.M. Sherif, D. Baleanu, An exact solution of a Casson fluid flow induced by dust particles with hybrid nanofluid over a stretching sheet subject to Lorentz forces, *Waves Random Complex Media*, pp. 1–14, 2022, <https://doi.org/10.1080/17455030.2022.2102689>.
14. C. Kumawat, B.K. Sharma, Q.M. Al-Mdallal, M. Rahimi-Gorji, Entropy generation for MHD two phase blood flow through a curved permeable artery having variable viscosity with heat and mass transfer, *Int. Commun. Heat Mass Transfer*, **133**:105954, 2022, <https://doi.org/10.1016/j.icheatmasstransfer.2022.105954>.
15. J.C. Lasheras, The biomechanics of arterial aneurysms, *Annu. Rev. Fluid Mech.*, **39**:293–319, 2007, <https://doi.org/10.1146/ANNUREV.FLUID.39.050905.110128>.
16. T.S. Lee, Steady laminar fluid flow through variable constrictions in vascular tube, *J. Fluids Eng.*, **116**(1):66–71, 1994, <https://doi.org/10.1115/1.2910244>.
17. T.R. Mahapatra, G.C. Layek, M.K. Maiti, Unsteady laminar separated flow through constricted channel, *Int. J. Non-Linear Mech.*, **37**(2):171–186, 2002, [https://doi.org/10.1016/S0020-7462\(00\)00104-9](https://doi.org/10.1016/S0020-7462(00)00104-9).
18. F. Mebarek-Oudina, I. Chabani, Review on nano-fluids applications and heat transfer enhancement techniques in different enclosures, *J. Nanofluids*, **11**(2):155–168, 2022, <https://doi.org/10.1166/jon.2022.1834>.
19. M. Nazeer, F. Hussain, M.I. Khan, K. Khalid, Theoretical analysis of electrical double layer effects on the multiphase flow of Jeffrey fluid through a divergent channel with lubricated walls, *Waves Random Complex Media*, 2022, <https://doi.org/10.1080/17455030.2022.2126025>.
20. S. Parvin, R. Nasrin, M.A. Alim, N.F. Hossain, A.J. Chamkha, Thermal conductivity variation on natural convection flow of water–alumina nanofluid in an annulus, *Int. J. Heat Mass Transfer*, **55**(19-20):5268–5274, 2012, <https://doi.org/10.1016/j.ijheatmasstransfer.2012.05.035>.
21. K.A. Powers, A.S. Dhmoon, Physiology, Pulmonary Ventilation and Perfusion, 2019, <https://www.ncbi.nlm.nih.gov/books/NBK539907/>.
22. J. Raza, F. Mebarek-Oudina, A.J. Chamkha, Magnetohydrodynamic flow of molybdenum disulfide nanofluid in a channel with shape effects, *Multidiscip. Model. Mater. Struct.*, **15**(4): 737–757, 2019, <https://doi.org/10.1108/MMMS-07-2018-0133>.
23. S.R.R. Reddy, Entropy generation on biomagnetic gold-copper/blood hybrid nanofluid flow driven by electrokinetic force in a horizontal irregular channel with bioconvection phenomenon, *Proc. Inst. Mech. Eng., Part C, J. Mech. Eng. Sci.*, **237**(7):1631–1646, 2022, <https://doi.org/10.1177/09544062221130018>.
24. S.R.R. Reddy, C.S.K. Raju, S.R. Gunakala, H.T. Basha, S.-J. Yook, Bio-magnetic pulsatile CuO–Fe<sub>3</sub>O<sub>4</sub> hybrid nanofluid flow in a vertical irregular channel in a suspension of body acceleration, *Int. Commun. Heat Mass Transfer*, **135**:106151, 2022, <https://doi.org/10.1016/J.ICHEATMASSTRANSFER.2022.106151>.
25. S.R.R. Reddy, P.B.A. Reddy, Thermal radiation effect on unsteady three-dimensional MHD flow of micropolar fluid over a horizontal surface of a parabola of revolution, *Propul. Power Res.*, **11**(1):129–142, 2022, <https://doi.org/10.1016/j.jprr.2022.01.001>.

26. S.R.R. Reddy, P.B.A. Reddy, A.J. Chamkha, Heat transfer analysis of MHD CNTs nanofluid flow over a stretching sheet, *Spec. Top. Rev. Porous Media, Int. J.*, **11**(2):133–147, 2020, <https://doi.org/10.1615/SpecialTopicsRevPorousMedia.2020030647>.
27. F. Selimefendigil, H.F. Öztop, A.J. Chamkha, Role of magnetic field on forced convection of nanofluid in a branching channel, *Int. J. Numer. Methods Heat Fluid Flow*, **30**(4):1755–1772, 2020, <https://doi.org/10.1108/HFF-10-2018-0568>.
28. B. Semlitsch, Y. Wang, M. Mihăescu, Flow effects due to pulsation in an internal combustion engine exhaust port, *Energy Convers. Manage.*, **86**:520–536, 2014, <https://doi.org/10.1016/J.ENCONMAN.2014.06.034>.
29. N. Shehzad, A. Zeeshan, M. Shakeel, R. Ellahi, S.M. Sait, Effects of magnetohydrodynamics flow on multilayer coatings of Newtonian and non-Newtonian fluids through porous inclined rotating channel, *Coatings*, **12**(4):430, 2022, <https://doi.org/10.3390/COATINGS12040430>.
30. D. Toghraie, R. Mashayekhi, H. Arasteh, S. Sheykhi, M. Niknejadi, A.J. Chamkha, Two-phase investigation of water- $\text{Al}_2\text{O}_3$  nanofluid in a micro concentric annulus under non-uniform heat flux boundary conditions, *Int. J. Numer. Methods Heat Fluid Flow*, **30**(4):1795–1814, 2019, <https://doi.org/10.1108/HFF-11-2018-0628>.
31. J.C. Umavathi, K. Hemavathi, Flow and heat transfer of composite porous medium saturated with nanofluid, *Propul. Power Res.*, **8**(2):173–181, 2019, <https://doi.org/10.1016/j.jprr.2019.01.010>.
32. S. Wang, G. Lu, Applications of gold nanoparticles in cancer imaging and treatment, in M.S. Seehra, A.D. Bristow (Eds.), *Noble and Precious Metals – Properties, Nanoscale Effects and Applications*, IntechOpen, 2017, <https://doi.org/10.5772/INTECHOPEN.70901>.